

Optimization of exciton currents in photosynthetic systems

Guan, Chengbo; Wu, Ning; Zhao, Yang

2013

Guan, C., Wu, N., & Zhao, Y. (2013). Optimization of exciton currents in photosynthetic systems. *The Journal of Chemical Physics*, 138(11).

<https://hdl.handle.net/10356/95792>

<https://doi.org/10.1063/1.4795204>

© 2013 American Institute of Physics. This paper was published in *The Journal of Chemical Physics* and is made available as an electronic reprint (preprint) with permission of American Institute of Physics. The paper can be found at the following official DOI: [<http://dx.doi.org/10.1063/1.4795204>]. One print or electronic copy may be made for personal use only. Systematic or multiple reproduction, distribution to multiple locations via electronic or other means, duplication of any material in this paper for a fee or for commercial purposes, or modification of the content of the paper is prohibited and is subject to penalties under law.

Downloaded on 20 Mar 2024 20:25:18 SGT

Optimization of exciton currents in photosynthetic systems

Chengbo Guan, Ning Wu, and Yang Zhao

Citation: *J. Chem. Phys.* **138**, 115102 (2013); doi: 10.1063/1.4795204

View online: <http://dx.doi.org/10.1063/1.4795204>

View Table of Contents: <http://jcp.aip.org/resource/1/JCPSA6/v138/i11>

Published by the American Institute of Physics.

Additional information on J. Chem. Phys.

Journal Homepage: <http://jcp.aip.org/>

Journal Information: http://jcp.aip.org/about/about_the_journal

Top downloads: http://jcp.aip.org/features/most_downloaded

Information for Authors: <http://jcp.aip.org/authors>

ADVERTISEMENT

physicstoday

Comment on any
Physics Today article.

The advertisement shows a screenshot of a *Physics Today* article titled "Measured energy in Japan" by David von Seggern. A red arrow points from the article to a comment box. The comment box contains a comment by Edgar McCarvill dated 14 July 2012 19:59, discussing the energy release of a 100-megaton explosion and the damage caused by a ball struck by a bat.

Optimization of exciton currents in photosynthetic systems

Chengbo Guan, Ning Wu, and Yang Zhao^{a)}

Division of Materials Science, Nanyang Technological University, Singapore 639798, Singapore

(Received 25 November 2012; accepted 27 February 2013; published online 19 March 2013)

In an approach analogous to that used to treat electronic currents in semiconductor quantum dots, we investigate the exciton current in a pigment network that is sandwiched between two exciton reservoirs, also known as the emitter and the acceptor. Employing the master equation for the reduced density matrix, the exciton current is obtained analytically for a two-site model, and numerically for an eight-site Fenna-Matthews-Olson (FMO) subunit model. It is found that, to maximize the exciton current with a specific network configuration, there exist optimal emitter temperatures and exciton transfer rates between the network and the reservoirs. The steady state current in the FMO model is consistent with the trapping time calculated by network optimization in the one-exciton picture. The current optimization with respect to various control parameters is discussed for the FMO model. At and below the biologically relevant transfer rate 1 ps^{-1} , the FMO network is more efficient for excitation energy transfer than the two-site model. Beyond this scale, the FMO network shows robustness with respect to the interplay with the reservoirs. © 2013 American Institute of Physics. [<http://dx.doi.org/10.1063/1.4795204>]

I. INTRODUCTION

Thanks to recent compelling experimental evidence of long-lived quantum coherence that facilitates excitation energy transfer (EET) in photosynthesis, considerable attention has been devoted to understanding the observed high EET efficiency in various complexes of chlorophylls (Chls) and bacteriochlorophylls (BChls).^{1–14} Among theoretical efforts are proposals using protein-protected (phonon-induced) coherence dynamics^{4–8} and network optimization.^{9–11} Most existing theoretical models are constructed using the one-exciton picture. In natural photosynthesis, the time scale of solar photon capture is much larger than those of excitation transfer and decay.^{15,16} Therefore, it perhaps makes sense to address the EET issues in the one-exciton picture. However, the process of EET in light-harvesting systems is one in which the excitons are successively created in antennas and trapped by reaction centers subsequently, yielding a continuous energy flow. Furthermore, for an artificial photosynthesis apparatus aimed to optimize solar energy utilization and improve photon capture efficiency, multi-exciton effects are not negligible, and the EET should be considered in a multi-exciton picture that is capable to describe continuous exciton currents. In fact, the creation and annihilation of excitons in the antennas and the reaction centers can be viewed as what occurs in sources and drains of energy carriers, respectively. Therefore, a new optimization mechanism is in need to better describe the source-drain transfer network of excitons. Along this line, Xiong *et al.* introduced a source-network-drain Hamiltonian¹⁴ for excitons to study EET in photosynthetic systems, analogous to treatments of electronic transport. The exciton current is calculated using the Landauer-Büttiker expression summing over all incident and outgoing exciton channels in the sources

and drains, respectively, and integrating over the energy.¹⁷ Effects of static disorder and thermal excitations on EET are examined by solving the Schrödinger equation and taking into account rates of exciton creations and annihilations in antennas and reaction centers as well as coherent exciton hoppings in the pigment network. A similar line will be followed in this work.

It is well known that in electronic transport processes the current can be described by the Green's function method¹⁸ or a quantum master equation approach¹⁹ among other theoretical tools. In this work, to deal with exciton transport in photosynthesis, we borrow the master equation method that has been widely used in the one-exciton picture. Making the Born-Markov approximation, we present the quantum master equation in the Lindblad form for exciton transfer processes between the pigments and the exciton emitter/acceptor with transfer rates given by the Fermi golden rule. Unlike electronic transport in quantum dots, the thermal average of the emitter exciton number plays a significantly different role in the excitation transfer dynamics. The average exciton number is directly related to the injection process, and behaves as a decoherence factor. From the experimentalist viewpoint, the average exciton number can be conveniently taken as the normalized temperature of the emitter. Our results indicate that, to maximize the exciton current (or quantum yield), there exist optimal emitter temperatures and transfer rates for a given molecular configuration. Taking into account the decay process of excitons, an analytic formulation for the steady state EET efficiency is given yielding a monotonically decreasing function of the normalized temperature.

We first investigate in this work the exciton current in a two-site toy model consisting of two coupled pigments as an exciton bridge between an emitter and an acceptor. Considering the emitter and the acceptor as exciton reservoirs, we focus on the exciton current in the steady state. Analogous to the electronic transport in semiconductor quantum dots,

^{a)}Electronic address: YZhao@ntu.edu.sg.

EET in excitonic conductors is treated by the master equation approach.²⁰ As an application of our formulation to a realistic network of BChls, we next discuss energy transfer in the well-known Fenna-Matthews-Olson (FMO) light harvesting complex in green sulfur bacteria.²¹ As an exciton conductor linking the chlorosome antennas to the reaction centers, the FMO consists of three identical subunits in which EET pathways are created by the BChl pigment-pigment coupling. Recent crystallographic analysis revealed a revised FMO structure with each subunit containing an eighth BChl in addition to the seven earlier-known BChls.^{22,23} Various non-Markovian and nonperturbative treatments have been suggested to model coherent EET in the seven-site monomer with BChl 1 or 6 initially excited.^{24–28} However, population oscillations that have been reported by a number of authors on the previously-known seven BChls may be suppressed by the eighth BChl due to a large difference in site energy of BChl 8 and weak coupling to the group of the seven BChls.^{29–31} Even without the short-time oscillations, the high EET efficiency is still preserved in the eight-site subunit. Moreover, the optimization theory proved that the FMO network was robust with respect to its own configuration and the interaction with the phonon bath.^{31,32} The exciton current optimization, with respect to the normalized temperature and the transfer rates, displays similar trends as in the two-site model. At and below the biological transfer rate 1 ps^{-1} , the FMO network is more efficient for EET than the two-site model.^{31,33} Beyond this scale, the FMO network shows robustness with respect to the interplay of the reservoirs. Following Ref. 31, the on-site energy of BChl 8 and the exciton-phonon coupling strength are discussed, and an optimal on-site energy of BChl 8 is found to be in good agreement with the experimental value. The exciton current is found to increase with the exciton-phonon coupling strength, before reaching saturation in a wide parameter regime.

The overdamped Brownian oscillator model in the high temperature limit^{5,24} with one of the frequently-used phonon correlation functions is employed in this work to help simulate phonon-induced dissipation under the Redfield approximation.^{34–37} Popular in nuclear magnetic resonance and optical spectroscopy, the Redfield approach treats the system-bath coupling to second order in perturbation theory, and uses the energy eigenstate representation with no promise of complete positivity. For all but the simplest cases, no analytical solutions can be found for the formidable Redfield equations. Under the assumption of Markovian dynamics and initial system-bath decoupling, the semigroup approach deals with dissipative dynamics by using the Lindblad dissipation operators, which are in fact operators in the system Hilbert space responsible for system-bath couplings. Semigroup methods can treat simultaneously multiple types of system-bath interactions. The Lindblad-type master equation widely used to describe exciton energy transfer in photosynthetic systems is the Haken-Strobl equation, also known as the Haken-Strobl-Lindblad equation.^{9,10,38–40} In this work, results on the population dynamics using the Haken-Strobl approximation⁴¹ are also presented for comparison. The Haken-Strobl model assumes infinite temperature, hence only the real part of the bath correlation function is kept. In the limit of vanishing exciton-band width, the Haken-

Strobl model can be recovered from the Redfield approximation. Numerical simulations show that the Redfield approach gives more reliable results as the interplay between pigment configurations and phonon relaxation is suppressed in the Haken-Strobl model. In the multi-exciton picture, by taking a biologically relevant transfer rate, the Redfield method yields a much larger outgoing current. Furthermore, the average trapping time from the Redfield simulation is consistent with that obtained in the one-exciton picture.³¹

In some biological light-harvesting systems such as the FMO complex, the exciton-phonon coupling (or the reorganization energy) is comparable in magnitude to the transfer coupling between pigments, which renders the conventional Redfield equation invalid for EET calculations.^{42,43} For this reason, many sophisticated theoretical treatments have been recently introduced, such as a few improved Redfield-like methods,^{40,44,45} the approach of polaron transformation combined with master equations,⁴⁶ the iterative path-integral algorithm,^{25,47} and the hierarchical equation of motion (HEOM) approach.^{5,24} Numerically exact quantum dynamics can be obtained by the latter two methods for hundreds of femtoseconds after the initial excitation, which are in agreement with earlier results in the weak- and strong-coupling regimes.^{25,47} In this work, however, we mainly concern ourselves with the steady state current and the long-time limit, and the Markovian approximation is therefore assumed. In the one-exciton picture, the conventional Redfield equation can reproduce approximately numerical results that are obtained by the HEOM approach and the path-integral algorithm in the long-time limit, as confirmed in Refs. 5 and 25. We expect similar conclusions to hold in the multi-exciton picture. Furthermore, the exciton Hilbert space in the multi-exciton picture is much larger than that in the one-exciton picture, rendering a rigorous investigation of phonon dissipation computationally expensive if not impossible. To capture the relevant optimization features of EET dynamics in a qualitative manner, we employ the Redfield-equation approach to discuss the phonon induced dissipation. More sophisticated treatments will be devised in our future efforts.

The remainder of our paper is organized as follows. In Sec. II, the master equation is introduced for the two-site model. An analytical form of the steady-state exciton current is obtained from the master equation together with the EET efficiency. In Sec. III, the relatively complicated FMO model is tackled numerically taking into account phonon induced dissipation. Optimization of the steady state current is discussed with respect to the normalized temperature, the transfer rates, the on-site energy of BChl 8, and the exciton-phonon coupling strength. Conclusions are drawn in Sec. IV.

II. EXCITON CURRENT IN THE TWO-SITE MODEL

In this section, we investigate a two-site system as an excitation conductor sandwiched between an emitter and an acceptor, as sketched in the upper panel of Fig. 1. The emitter and acceptor are treated as uncorrelated exciton reservoirs, and assumed to be always in thermal equilibrium with chemical potentials μ_E and zero, respectively. The Hamiltonian of

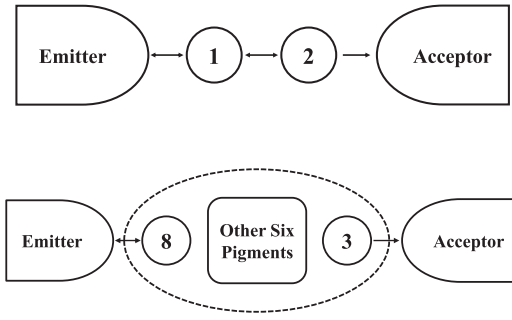


FIG. 1. Schematic illustration of the exciton conduction in a two-site toy model (upper panel) and that in an eight-site FMO subunit (lower panel). The exciton transfer from emitters to sites is reversible, whereas the transfer from sites to acceptors is irreversible. Our calculations indicate that the FMO network provides a larger exciton current than the two-site model, for the biological transfer rate $\gamma = 1 \text{ ps}^{-1}$.

the entire system is given by

$$\hat{H} = \hat{H}_S + \hat{H}_R + \hat{H}_{SR}, \quad (1)$$

where

$$\hat{H}_S = \sum_{n=1}^2 E_n \hat{c}_n^\dagger \hat{c}_n - J(\hat{c}_1^\dagger \hat{c}_2 + \hat{c}_2^\dagger \hat{c}_1), \quad (2)$$

$$\hat{H}_R = \sum_k \varepsilon_k \hat{e}_k^\dagger \hat{e}_k + \sum_p \epsilon_p \hat{a}_p^\dagger \hat{a}_p, \quad (3)$$

$$\begin{aligned} \hat{H}_{SR} = & \sum_k [T_E(\varepsilon_k) \hat{c}_1^\dagger \hat{e}_k + T_E^*(\varepsilon_k) \hat{c}_1 \hat{e}_k^\dagger] \\ & + \sum_p [T_A(\epsilon_p) \hat{c}_2^\dagger \hat{a}_p + T_A^*(\epsilon_p) \hat{c}_2 \hat{a}_p^\dagger]. \end{aligned} \quad (4)$$

Here \hat{H}_S denotes the pure exciton Hamiltonian of the two-site system, where each site is a two-level system represented by the on-site energy E_n and the Frenkel exciton annihilation (creation) operator \hat{c}_n (\hat{c}_n^\dagger); J is the hopping integral between the two sites. The reservoir Hamiltonian is labeled by \hat{H}_R , where ε_k (ϵ_p) and \hat{e}_k (\hat{a}_p) denote the single-particle energy and the annihilation operator of the emitter (acceptor), respectively. The interaction between the system and reservoirs, \hat{H}_{SR} , is described by the electronic coupling coefficients T_E and T_A , which in general depend on the energy levels of the corresponding excitation bands.

We assume weak transmission and that the relaxation time scales of both reservoirs are much smaller than that for inter-site hopping. Following the standard second-order perturbation theory, and making the Markov approximation, the master equation of the reduced density matrix $\rho = \text{Tr}_R\{\rho^{\text{tot}}\}$ can be written in the Lindblad form^{20,48–51} (here \hbar is set to unity)

$$\begin{aligned} \frac{d\rho}{dt} = \mathcal{L}\rho = & -i[\hat{H}_S, \rho] \\ & + \frac{1}{2}\gamma_E \bar{n}_E [2\hat{c}_1^\dagger \rho \hat{c}_1 - \rho \hat{c}_1 \hat{c}_1^\dagger - \hat{c}_1 \hat{c}_1^\dagger \rho] \\ & + \frac{1}{2}\gamma_E (1 + \bar{n}_E) [2\hat{c}_1 \rho \hat{c}_1^\dagger - \rho \hat{c}_1^\dagger \hat{c}_1 - \hat{c}_1^\dagger \hat{c}_1 \rho] \\ & + \frac{1}{2}\gamma_A [2\hat{c}_2 \rho \hat{c}_2^\dagger - \rho \hat{c}_2^\dagger \hat{c}_2 - \hat{c}_2^\dagger \hat{c}_2 \rho]. \end{aligned} \quad (5)$$

Here the first term on the right hand side denotes the inter-site exciton hopping, and the remaining three terms describe the Poisson processes^{52–54} that correspond to the exciton injection from the emitter to site 1, the exciton reflection from site 1 to the emitter, and the exciton transmission from site 2 to the acceptor. Further, γ_E and γ_A are the injection and transmission rates, respectively, which are determined by the Fermi golden rule,²⁰

$$\gamma_E = 2\pi |T_E(E_1)|^2 \mathcal{Q}_E(E_1),$$

$$\gamma_A = 2\pi |T_A(E_2)|^2 \mathcal{Q}_A(E_2),$$

where \mathcal{Q}_E and \mathcal{Q}_A are the densities of states of the corresponding reservoirs. In this paper, γ_E and γ_A are called as the transfer rates for the emitter and acceptor, respectively. \bar{n}_E is the average emitter exciton number in a degenerate state of the energy level E_1 ,

$$\bar{n}_E = \frac{1}{e^{(E_1 - \mu_E)/k_B T} - 1}.$$

Ultra-low temperatures and the Bose-Einstein condensation are beyond the scope of this paper. One can expect that the chemical potential μ_E varies slowly near the physiological temperature and does not deviate too far from the on-site energy (e.g., hundreds of cm^{-1}), and thus, the mean exciton number is effectively related to the temperature.⁵⁵ Since \bar{n}_E increases monotonically with T , \bar{n}_E can be considered as the normalized temperature of the emitter. In the acceptor, the chemical potential is assumed to be zero so that the mean exciton number can be neglected if the temperature is not very high.

There are four bases in the site representation: the exciton vacuum state $|0\rangle \equiv |0, 0\rangle$, the singly excited states $|1\rangle \equiv |1, 0\rangle$, $|2\rangle \equiv |0, 1\rangle$, and the doubly occupied state $|d\rangle \equiv |1, 1\rangle$. The exciton populations $P_1 \equiv \text{Tr}\{\rho \hat{c}_1^\dagger \hat{c}_1\}$ and $P_2 \equiv \text{Tr}\{\rho \hat{c}_2^\dagger \hat{c}_2\}$, and the exciton coherence $\rho_{12} = \text{Tr}\{\rho \hat{c}_2^\dagger \hat{c}_1\}$ obeys a closed set of equations,

$$\frac{dP_1}{dt} = 2J\text{Im}\rho_{12} + \gamma_E \bar{n}_E (1 - P_1) - \gamma_E (1 + \bar{n}_E) P_1, \quad (6)$$

$$\frac{dP_2}{dt} = -2J\text{Im}\rho_{12} - \gamma_A P_2, \quad (7)$$

$$\begin{aligned} \frac{d\rho_{12}}{dt} = & -i[E_{12}\rho_{12} + J(P_1 - P_2)] \\ & - \gamma_E \bar{n}_E \rho_{12} - \frac{1}{2}(\gamma_E + \gamma_A)\rho_{12}. \end{aligned} \quad (8)$$

Here “Im” denotes the imaginary part of a complex variable, and $E_{12} \equiv E_1 - E_2$ is the on-site energy difference (i.e., detuning). On the right side of equation (7), the first term describes the hopping from site 1 to site 2, and the second term, the transfer from site 2 to the acceptor. Naturally, one can define the average outgoing current as

$$\langle I_o \rangle = \gamma_A P_2, \quad (9)$$

which quantifies the exciton current from the system to the acceptor, or the quantum yield in a unit time. Similarly, the average incoming current can be defined as

$$\langle I_{in} \rangle = \gamma_E \bar{n}_E (1 - P_1) - \gamma_E (1 + \bar{n}_E) P_1. \quad (10)$$

From this point on, the average outgoing current $\langle I_o \rangle$ is referred to as the exciton current without ambiguity. Given an initial state, one can solve the master equation exactly. However, for long times, the system settles into a steady state that has no memory of initial conditions. In the steady state, Eqs. (6)–(8) are reduced to algebraic equations that can be solved easily,

$$P_1^\infty = \frac{\bar{n}_E - P_2^\infty \gamma_A / \gamma_E}{2\bar{n}_E + 1}, \quad (11)$$

$$P_2^\infty = \frac{2J^2 \Omega \gamma_E \bar{n}_E}{(2\bar{n}_E + 1)(E_{12}^2 + \Omega^2) \gamma_E \gamma_A + 4J^2 \Omega^2}, \quad (12)$$

$$\rho_{12}^\infty = -\left(\frac{E_{12}}{\Omega} + i\right) \frac{\gamma_A P_2^\infty}{2J}, \quad (13)$$

where the upper index “ ∞ ” indicates the steady state and $\Omega \equiv \gamma_E(\bar{n}_E + 1/2) + \gamma_A/2$. The real part of ρ_{12}^∞ depends on the on-site energy difference E_{12} , and its imaginary part is directly proportional to the exciton current, pointing to the fact that an enhanced coherence brings about more efficient energy transport.

For a system with parity, $E_{12} = 0$ and $\gamma_A = \gamma_E = \gamma$, the exciton current has a simplified form $\langle I_o \rangle^\infty$ in the steady state,

$$\langle I_o \rangle^\infty = \frac{2J^2 \gamma \bar{n}_E}{(\bar{n}_E + 1)[(2\bar{n}_E + 1)\gamma^2 + 4J^2]}. \quad (14)$$

Up to a saturation value, the exciton current trivially increases with the hopping integral J ,

$$\langle I_o \rangle^\infty|_{J^2/\gamma^2 \gg \bar{n}_E} = \frac{\bar{n}_E \gamma}{2(\bar{n}_E + 1)}. \quad (15)$$

But for a given J , there exist optimal values of \bar{n}_E and γ ,

$$\bar{n}_E = \frac{1 + \sqrt{5}}{2} \simeq 1.62, \quad \gamma = 2J\sqrt{\sqrt{5} - 2} \simeq 0.97J, \quad (16)$$

which maximize the steady current. In Fig. 2, the steady state current $\langle I_o \rangle^\infty$ is plotted as a function of the normalized temperature \bar{n}_E and the normalized transfer rate γ/J . As the

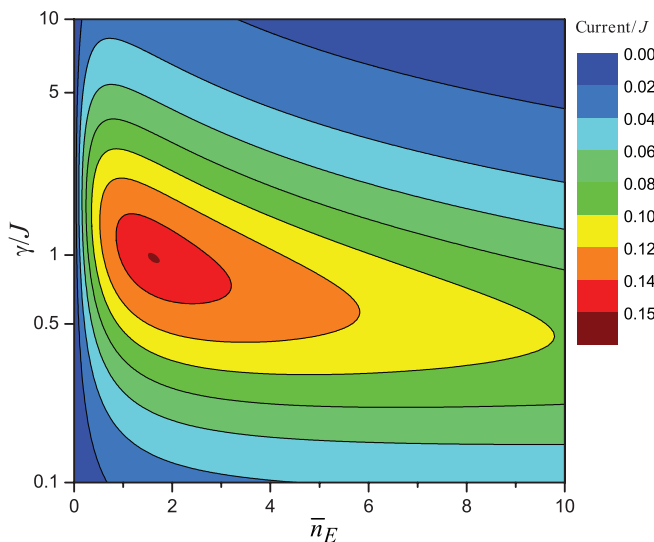


FIG. 2. Steady-state exciton current $\langle I_o \rangle^\infty$ versus γ/J and \bar{n}_E in the symmetric two-site model. The temperature dependence of the current varies dramatically while the transfer rates take values around the hopping integral.

temperature (or the transfer rate) goes up, the current firstly increases quickly reaching a maximum, and then decreases gradually. In Eq. (6), the factor $\gamma \bar{n}_E$ plays the role of excitation injection rate, but in Eq. (8), it is tied to decoherence. For large transfer rates or at high temperatures, the decoherence effect becomes dominant, and the exciton current is suppressed.

To define the EET efficiency, we introduce the decay process with a homogeneous decay rate γ_d . Exciton population decay per unit time is given by $\langle I_d \rangle = \gamma_d(P_1 + P_2)$. In the steady state, $\langle I_{in} \rangle^\infty = \langle I_o \rangle^\infty + \langle I_d \rangle^\infty$, and the EET efficiency is defined as

$$\eta^\infty = \frac{\langle I_o \rangle^\infty}{\langle I_o \rangle^\infty + \langle I_d \rangle^\infty} = \frac{1}{1 + \frac{\gamma_d}{\gamma} \left(\frac{P_1^\infty}{P_2^\infty} + 1 \right)}. \quad (17)$$

In principle, the decay process may be involved in the master equation. However, as γ_d is much smaller than the transfer rates and hopping integral, the steady state populations differ very little from those given in Eqs. (11) and (12). Neglecting higher order terms (in γ_d/γ), one can substitute Eqs. (11) and (12) into Eq. (17), and obtain

$$\eta^\infty = \frac{1}{1 + 2\frac{\gamma_d}{\gamma} + \frac{\gamma \gamma_d}{2J^2}(\bar{n}_E + 1)}. \quad (18)$$

As expected, the EET efficiency decreases monotonically as the normalized temperature goes up. The reason is that, for a given transfer rate γ , a larger n_E means more injected exciton populations to occupy the conductor before the decay process.

III. EXCITON CURRENT IN THE FMO MODEL

Realistic systems in photosynthesis have of course more than two pigments. For example, there are 7 or 8 pigments in the much studied FMO complex of green sulfur bacteria, whereas the LH2 complex of *R. Acidophila* has two rings of chromophores, one with 18 sites and one with nine. In this section, we choose an eight-site FMO subunit as the conductor between an artificial exciton emitter and an acceptor. An illustration is shown in the lower panel of Fig. 1, wherein BChls 8 and 3 serve as the entrance and the exit, respectively.^{29–31} In the FMO complex, the BChl pigments are strongly coupled to the surrounding protein matrix. Hence the dissipation caused by the exciton-phonon scattering should be considered.

The system Hamiltonian \hat{H} is given as

$$\hat{H} = \hat{H}_S + \hat{H}_B + \hat{H}_{SB} + \hat{H}_R + \hat{H}_{SR}, \quad (19)$$

$$\hat{H}_S = \sum_{n=1}^8 (E_n + \lambda_n) \hat{c}_n^\dagger \hat{c}_n + \sum_{m \neq n} J_{mn} \hat{c}_m^\dagger \hat{c}_n, \quad (20)$$

$$\hat{H}_B = \sum_{n,\xi} \frac{1}{4} \omega_\xi (\hat{P}_{n\xi}^2 + \hat{Q}_{n\xi}^2), \quad (21)$$

$$\hat{H}_{SB} = \sum_n \hat{c}_n^\dagger \hat{c}_n \hat{u}_n, \quad \hat{u}_n = - \sum_\xi \omega_\xi g_{n\xi} \hat{Q}_{n\xi}. \quad (22)$$

Here \hat{H}_S is the exciton Hamiltonian of the eight-site subunit characterized by the on-site energies E_n and hopping

integrals J_{mn} . Each pigment is coupled to its local environmental phonon bath, which is described by harmonic oscillators with various modes in \hat{H}_B , where ω_ξ and $\hat{Q}_{n\xi}$ ($\hat{P}_{n\xi}$) denote the frequency and dimensionless canonical coordinate (momentum) of the ξ -mode, respectively. \hat{H}_{SB} depicts the linear exciton-phonon coupling, in which $g_{n\xi}$ is the coordinate shift of the equilibrium configuration of the ξ -mode, between the ground and excited states of the n th site.⁵⁶ $\lambda_n \equiv \sum_\xi g_{n\xi}^2 \omega_\xi$ is the reorganization energy that characterizes the exciton-phonon coupling strength. Finally, the reservoir Hamiltonian \hat{H}_R and the system-reservoir interaction Hamiltonian \hat{H}_{SR} assume the same forms as those in Eqs. (3) and (4) in the two-site model.

The master equation of the reduced density matrix, $\rho = \text{Tr}_{R,B}\{\rho^{\text{tot}}\}$, can be generally written as

$$\frac{d\rho}{dt} = \mathcal{L}\rho = \mathcal{L}_S\rho + \mathcal{L}_{SR}\rho + \mathcal{L}_{SB}\rho. \quad (23)$$

$\mathcal{L}_S\rho$ describes the free exciton evolution, and $\mathcal{L}_{SR}\rho$, the injection-emission process, similar to Eq. (5). Accordingly, the average outgoing current and the steady state EET efficiency can be defined by

$$\langle I_o \rangle = \gamma_A P_3, \quad (24)$$

$$\eta^\infty = \frac{\langle I_o \rangle^\infty}{\langle I_o \rangle^\infty + \langle I_d \rangle^\infty} = \frac{\langle I_o \rangle^\infty}{\langle I_o \rangle^\infty + \gamma_d \sum_{\alpha=1}^8 P_\alpha^\infty}, \quad (25)$$

where γ_A and γ_d are the emission (trapping) rate and the homogeneous decay rate, respectively; $P_\alpha \equiv \text{Tr}\{\rho \hat{c}_\alpha^\dagger \hat{c}_\alpha\}$ is the exciton population on site α .

The last term on the right side of Eq. (23) represents the dissipation process induced by the exciton-phonon scattering. Since we are interested in the steady state, the Markov approximation can be readily used. Our starting point is the second order cumulant expansion in the Markovian and secular limits,^{5,56–58}

$$\mathcal{L}_{SB}\rho = - \sum_n [\hat{c}_n^\dagger \hat{c}_n, \hat{\Lambda}_n \rho - \rho \hat{\Lambda}_n^\dagger], \quad (26)$$

$$\hat{\Lambda}_n = \int_0^\infty d\tau C_n(\tau) e^{-i\hat{H}_S\tau} \hat{c}_n^\dagger \hat{c}_n e^{i\hat{H}_S\tau}. \quad (27)$$

Dissipation is characterized by the time correlation function of the phonon bath,

$$C_n(t) = \sum_\xi g_{n\xi}^2 \omega_\xi^2 \left[\coth\left(\frac{\omega_\xi}{2k_B T}\right) \cos \omega_\xi t - i \sin \omega_\xi t \right]. \quad (28)$$

The simplest treatment of the correlation function is the δ -correlation assumption,⁴¹ $C_n(t) \sim \delta(t)$, which leads to the Haken-Strobl form,^{9,10}

$$\mathcal{L}_{SB}\rho = - \sum_n \eta_n [\hat{c}_n^\dagger \hat{c}_n \rho + \rho \hat{c}_n^\dagger \hat{c}_n - 2\hat{c}_n^\dagger \hat{c}_n \rho \hat{c}_n^\dagger \hat{c}_n], \quad (29)$$

where η_n denotes the dissipation rate. Such a simplification has an obvious shortcoming that the dependence of the dissipation rate on the physical parameters (e.g., the temperature) is not clear.

A more precise treatment is to extract the correlation function from fitting measured spectra. One frequently used form is the overdamped Brownian oscillation in the high temperature limit,^{5,32,33,59–62}

$$C_n(t) = (2\lambda_n k_B T - i\lambda_n \omega_c) e^{-\omega_c t}, \quad \text{for } T > T_c. \quad (30)$$

where ω_c and $T_c \equiv \hbar\omega_c/k_B$ are the characteristic frequency and temperature of the phonon bath, respectively. With this correlation function, Eq. (27) can be readily expressed in the exciton basis,

$$\hat{\Lambda}_n = \sum_{\mu,\nu} \frac{2\lambda_n k_B T - i\lambda_n \omega_c}{\omega_c + i\omega_{\mu\nu}} A_{n\mu}^* A_{n\nu} \hat{c}_\mu^\dagger \hat{c}_\nu, \quad (31)$$

$$\hat{c}_\mu^\dagger = \sum_n A_{n\mu} \hat{c}_n^\dagger, \quad \hat{H}_S = \sum_\mu \epsilon_\mu \hat{c}_\mu^\dagger \hat{c}_\mu, \quad (32)$$

where $\omega_{\mu\nu} = \epsilon_\mu - \epsilon_\nu$ is the exciton energy difference. Substituting Eq. (31) into Eq. (26), one obtains the secular Redfield form.

If the free exciton bandwidth is much smaller than the relaxation rate of the phonon bath, i.e., $\omega_{\mu\nu} \ll \omega_c$, the Redfield approximation can be reduced to the Haken-Strobl form

$$\hat{\Lambda}_n \simeq (2\lambda_n T/T_c - i\lambda_n) \hat{c}_n^\dagger \hat{c}_n. \quad (33)$$

On the right hand side of Eq. (33), the real part of the coefficient, $2\lambda_n T/T_c$, is the temperature-dependent dissipation rate η_n , and the imaginary part cancels out the on-site energy shift in \hat{H}_S . However, this is not the case for the FMO complex. The phonon parameters used are $\lambda_n = \lambda_c = 35 \text{ cm}^{-1}$, and $\omega_c = (50 \text{ fs})^{-1}$ is of the same order of magnitude as the exciton bandwidth.^{24,31,63,64} The value of $(50 \text{ fs})^{-1}$ has been widely used as the cutoff frequency in the literature.^{31,42} In the calculations below, we will employ (λ_c, ω_c) for the phonon manifold and (E_n, J_{mn}) for the pigment network following Renger and co-workers.²⁹ The temperature of the phonon bath is set to be 300 K, which is higher than the characteristic temperature $T_c = 153 \text{ K}$, thus satisfying the high temperature condition. The decay rate is set to be $\gamma_d = 1 \text{ ns}^{-1}$, and for simplicity, the transfer rates are assumed to be uniform $\gamma_E = \gamma_A = \gamma$.

The interplay between the pigment configuration and phonon bath relaxation is suppressed in the Haken-Strobl model (33), which inevitably leads to inferior results when compared with those obtained under the Redfield approximation (31). In Fig. 3, we present population dynamics in the one-exciton picture calculated by the two approaches. There is an acceptor but no emitter source, and initially BChl 8 is excited. One can see that the exciton populations fade away within ten picoseconds in the Redfield approach, whereas in the Haken-Strobl simulation the populations reach the thermal equilibrium and last for a much longer period of time. In comparison, both the emitter and the acceptor are present in the multi-exciton picture, and all the pigments are initially in their ground states. As shown in Fig. 4, the exciton populations calculated by the two approaches in the multi-exciton picture increase with the time until the steady state is reached. Using a biologically relevant transfer rate $\gamma = 1 \text{ ps}^{-1}$, it is revealed that the exciton currents calculated by the two

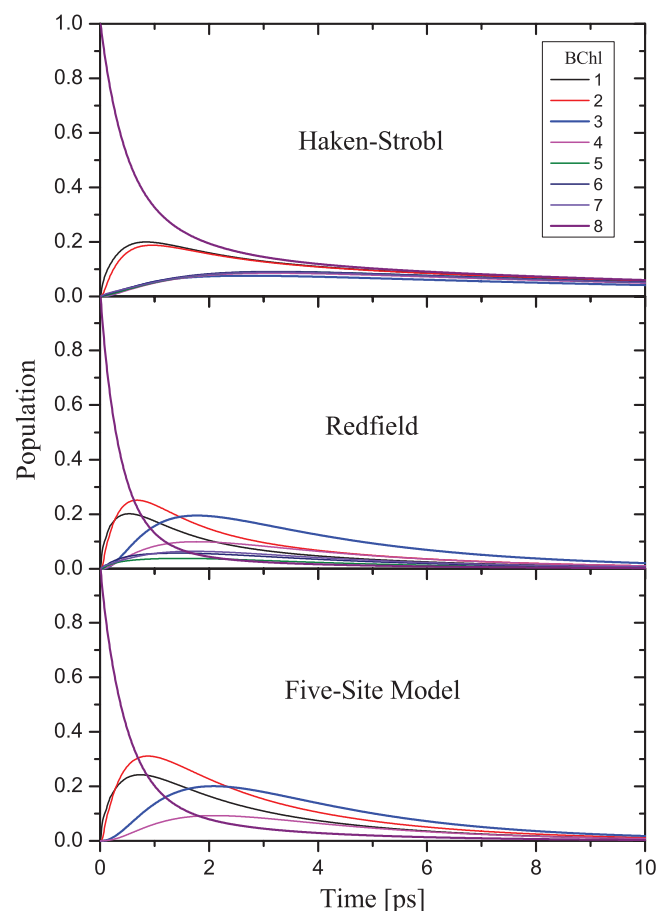


FIG. 3. The FMO population dynamics in the one-exciton picture with BChl 8 excited initially. The upper and middle panels display results from the eight-site model using the Haken-Strobl and Redfield approaches, respectively. The bottom panel shows results from the five-site model using the Redfield approach.

methods are very different. As shown in Fig. 4 by the thicker blue lines next to the “current” label, the Redfield method yields a much larger exciton current than the Haken-Strobl approach. It should be noted that the steady state exciton current 0.3 ps^{-1} obtained in the Redfield simulation corresponds to an average transfer time 3.3 ps for one exciton to go from the emitter to the acceptor, a result that is consistent with the trapping time scale in the one-exciton picture.³¹

There are two well-known EET pathways in the traditional seven-site FMO monomer which correspond to two distinct entry sites (1 and 6) and accept excitation energy from the chlorosome with equal priorities.^{65–67} In the eight-site scenario, site 8 is the most likely entry point because of its location and orientation. Considering the coupling strengths between BChl 8 and the other sites, there exists a dominant pathway that starts from BChl 8, goes through BChls 1 and 2, and terminates at BChl 3. This can be seen from the population dynamics in the one-exciton picture, in which those dominant sites attract most of the exciton population till the exciton is trapped to the reaction center. Among others, BChl 4 is the only pigment that couples strongly to the dominant exciton pathway. Thus, a reduced five-site model (the four-pigment pathway plus site 4) can be adopted to simplify numerical calculations.³¹ In the bottom panels of Figs. 3 and 4,

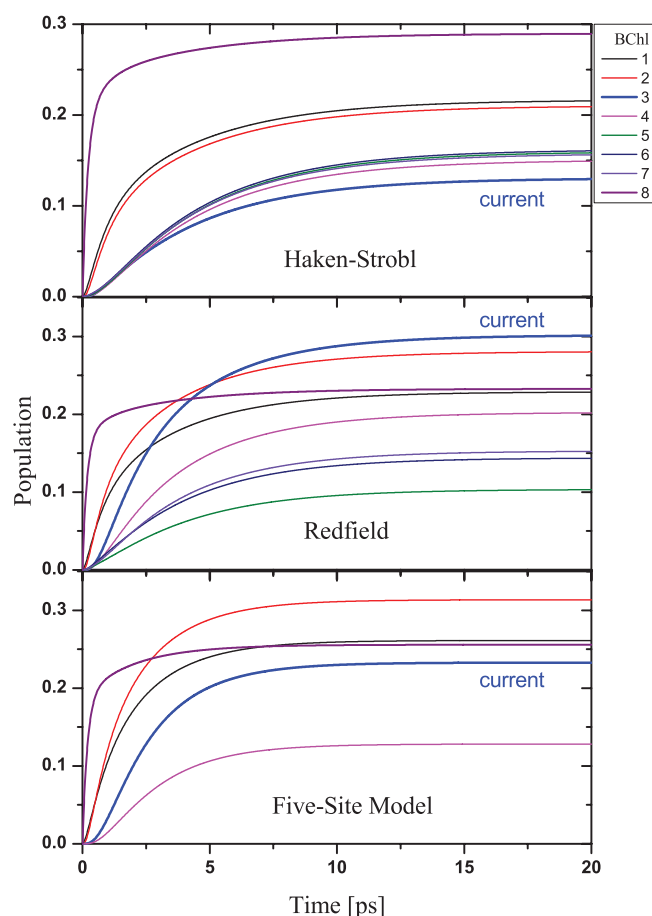


FIG. 4. The FMO population dynamics in the multi-exciton picture with all 8 pigments in the ground states. See line-color labels in Fig. 3. Here we set $\bar{n}_E = 1$ and $\gamma = 1 \text{ ps}^{-1}$, hence the exciton current in the multi-exciton picture equals to the population $P_3 \equiv \text{Tr}[\rho \hat{c}_3^\dagger \hat{c}_3]$ in unit of ps^{-1} , which is shown as the thicker blue lines next to the “current” label in the three panels.

population dynamics is displayed for the five-site model using the Redfield method. In the one-exciton picture, results differ only slightly from the eight-site model. In contrast, the distinction is substantial in the multi-exciton picture, as demonstrated by the population on site 3, thus leading to the claim that the rest four BChls in FMO, i.e., sites 4, 5, 6, and 7, may help build an auxiliary pathway for interference-enhanced exciton transport in the eight-site FMO conductor.

Now we concentrate on the steady state exciton current and its optimization in the eight-site FMO model within the Redfield framework. The steady state density matrix is constrained by

$$\mathcal{L}\rho^\infty = \lim_{t \rightarrow \infty} \frac{d\rho}{dt} = 0, \quad (34)$$

$$\text{Tr}\rho^\infty = 1. \quad (35)$$

In the Liouville space, the steady state density matrix ρ^∞ is a normalized eigenvector of the super-operator \mathcal{L} with zero eigenvalue. For the eight-site exciton system, the dimension of the Hilbert space is 2^8 , and the dimension of the Liouville space is 2^{16} , making it difficult to solve Eq. (34) by direct diagonalization of \mathcal{L} . An alternative method is to solve the master equation (23) for a sufficiently long time so that the

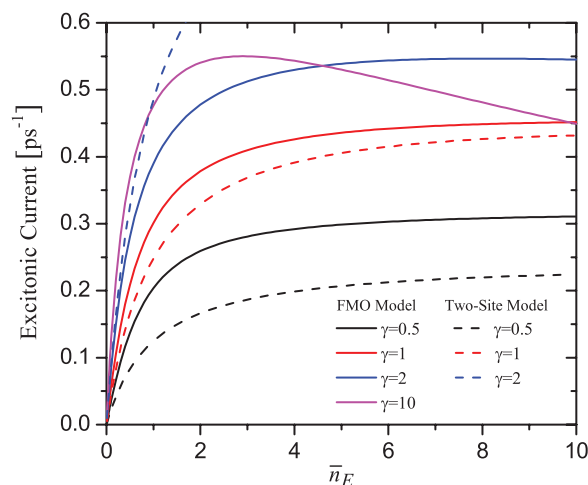


FIG. 5. The exciton current versus \bar{n}_E in the FMO model (solid lines) and two-site model (dashed lines), for various transfer rates γ in units of ps^{-1} . The hopping integral J in the two-site model is set to be 10 ps^{-1} .

first derivative of the density matrix converges to zero within a given precision. In our calculations, the precision requirement is set to be $\|\mathcal{L}\rho^\infty\| < 10^{-6} \text{ ps}^{-1}$.

Figure 5 presents the steady state exciton current as a function of the normalized temperature of the emitter. In the FMO model, when the transfer rates are much smaller than the average pigment-pigment coupling strength ($\sim 10 \text{ ps}^{-1}$), the current increases with the temperature before reaching saturation in a wide parameter regime. As the transfer rates are increased to the average hopping integral, optimal value for the normalized temperature appears readily. The above behavior is similar to that of the two-site model. To give a comparison between these two models, we match the hopping integral in the two-site model to the average hopping integral of the FMO model, and the corresponding current-temperature curves are shown in Fig. 5. It is found that the FMO model provides larger currents than the two-site model, at or below the biological transfer rate scale 1 ps^{-1} , whereas for $\gamma > 1 \text{ ps}^{-1}$, an opposite trend is revealed. This points to that the FMO network is perhaps optimized for weak coupling to the antenna and the reaction center. It should be noted that the FMO network is more robust than the streamlined two-site model for $\bar{n}_E > 1$.

The robustness of the FMO network is further demonstrated in Fig. 6, where the steady state exciton current and the EET efficiency plotted as functions of the transfer rate. It can be seen that at low to moderate temperatures the current in the FMO model increases slowly with γ for $\gamma > 1 \text{ ps}^{-1}$. For high temperatures, the optimal γ which maximizes the current emerges around the biologically relevant value. However, in the two-site model the exciton current changes dramatically with the transfer rates in a wide parameter regime as shown in Fig. 2, while the EET efficiency monotonically increases with the transfer rates. For $\gamma > 1 \text{ ps}^{-1}$, the temperature dependence of EET is negligible.

The exciton current provides us a new way for optimization not only on the interplay between the pigment network and the emitter/acceptor, but also on the configuration of the network itself. For an example, Fig. 7 displays the dependence

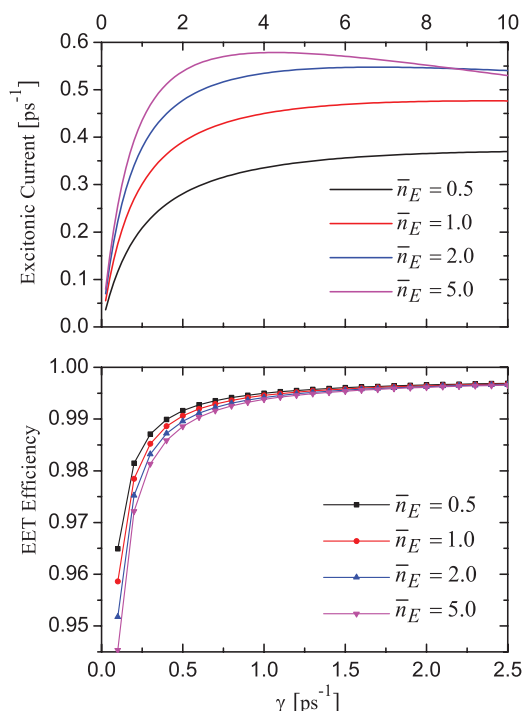


FIG. 6. The exciton current (upper panel) and the EET efficiency (lower panel) as functions of γ in the FMO model, for various normalized temperatures. The FMO model is robust as the transfer rates go beyond the biological scale.

of the exciton current on the on-site energy of BChl 8. It is found that the optimal on-site energies are close to the experimental value 700 cm^{-1} for several transfer rates, and as the transfer rate decreases, the optimal energy moves higher and closer toward 700 cm^{-1} .

It has been demonstrated in the literature that the protein environment plays a crucial role in determining the EET efficiency in light harvesting complexes. Figure 8 shows the dependence of the exciton current on the exciton-phonon coupling strength in the FMO model. It is apparent in Fig. 8 that the exciton current increases with the exciton-phonon coupling if its strength stays below $\lambda_c = 35 \text{ cm}^{-1}$. This result

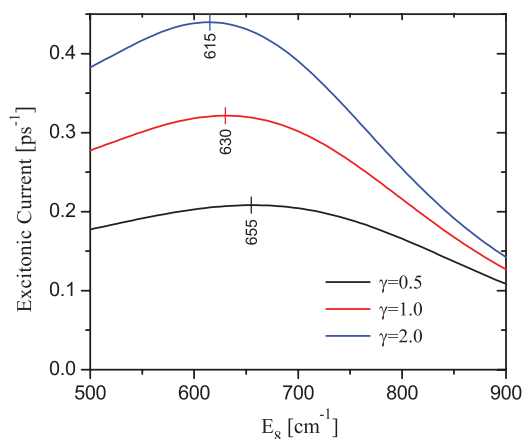


FIG. 7. Exciton current (in ps^{-1}) versus on-site energy (in cm^{-1}) of BChl 8 in the FMO model, for various transfer rates γ in units of ps^{-1} . Optimal on-site energies are marked for each curve. The reference of on-site energies is 12000 cm^{-1} .

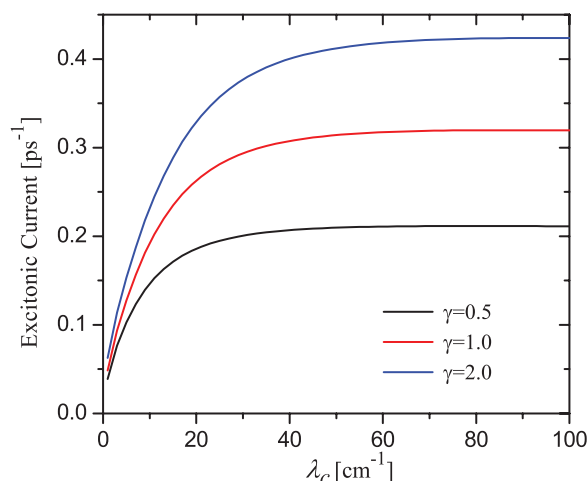


FIG. 8. Exciton current (in ps^{-1}) versus exciton-phonon coupling strength (in cm^{-1}) in the FMO model for various transfer rates γ in units of ps^{-1} . The robustness is also shown when the coupling strength goes beyond 35 cm^{-1} .

is in agreement with that obtained previously by Xiong *et al.*¹⁴ for a photosynthetic source-network-drain system using a time-dependent Schrödinger equation approach, in which the exciton current at $T = 300 \text{ K}$ is found to increase monotonically with the exciton-phonon coupling strength if it is smaller than 48 cm^{-1} . Deviation of our result from that in Ref. 14 in the strong-coupling regime is attributed to the breakdown of the Redfield approximation outside the weak-coupling regime. While on-site energy variations can enable the pigment network to absorb at a broad range of frequencies,⁶⁸ exciton-phonon interactions help broaden the spectral lines further forming an excitation energy funnel.²⁹ Dynamic disorder may scatter exciton transport and impeded energy transfer, but the phonon modes can also supply alternative channels for exciton transport facilitating energy transfer.

Finally, as mentioned in the Introduction, we note that despite being a simplified treatment that comes with analytical expressions and a physically intuitive picture of the dynamics, the Redfield approach used here neglects several important aspects crucial for a quantitative description of the quantum dissipative process, such as the memory of the thermal bath and strong-coupling effects. Future extension to the non-Markovian regime is necessary to arrive at a more accurate description of the quantum dissipative process.

IV. CONCLUSIONS AND REMARKS

Using approaches analogous to those employed to treat electronic currents in semiconductor quantum dots, we have studied the exciton current in a pigment network sandwiched between two exciton reservoirs. The exciton transfer process between the pigment and the exciton reservoir is treated within the Lindblad form, while the phonon-induced dissipation process is approximated in the secular Redfield description. In contrast to the quantum yield in the one-exciton picture, the exciton current in the multiple-exciton picture provides a new venue for optimization on pigment configurations and pigment-environment interplays. Employing the master equation for the reduced density matrix, the exciton

current is obtained analytically for a two-site model, and numerically for an eight-site FMO subunit model. Given a specific conductor configuration there exist optimal emitter temperatures and transfer rates that maximize the exciton current. The steady state current in the FMO model is consistent with the trapping time calculated by network optimization in the one-exciton picture. Optimization with respect to various control parameters is discussed for the FMO model, which is shown to be an efficient, robust network for the excitation energy transfer. Finally, we mention some recent work by Manzano,⁶⁹ which also addresses steady-state EET optimization in systems similar to ours. Using the master equation method, Manzano calculated the energy and exciton flux in a seven-site FMO model with fixed transfer rates $\gamma \simeq 0.2 \text{ ps}^{-1}$. The dissipation process is treated with the Haken-Strobl method and the optimization focuses on dissipation rates and Hamiltonian disorder. Optimal dissipation rates were found to be around 60 cm^{-1} for FMO.

ACKNOWLEDGMENTS

Support from the Singapore National Research Foundation through the Competitive Research Programme (CRP) under Project No. NRF-CRP5-2009-04 is gratefully acknowledged.

- ¹G. S. Engel *et al.*, *Nature (London)* **446**, 782 (2007).
- ²H. Lee, Y. C. Cheng, and G. R. Fleming, *Science* **316**, 1462 (2007).
- ³G. Panitchayangkoon *et al.*, *Proc. Natl. Acad. Sci. U.S.A.* **107**, 12766 (2010).
- ⁴A. Olaya-Castro *et al.*, *Phys. Rev. B* **78**, 085115 (2008).
- ⁵A. Ishizaki and G. R. Fleming, *J. Chem. Phys.* **130**, 234111 (2009).
- ⁶A. Nazir, *Phys. Rev. Lett.* **103**, 146404 (2009).
- ⁷S. Jang, *J. Chem. Phys.* **135**, 034105 (2011).
- ⁸A. W. Chin, S. F. Huelga, and M. B. Plenio, *Philos. Trans. R. Soc. London, Ser. A* **370**, 3638 (2012).
- ⁹F. Caruso *et al.*, *J. Chem. Phys.* **131**, 105106 (2009).
- ¹⁰J. S. Cao and R. J. Silbey, *J. Phys. Chem. A* **113**, 13825 (2009).
- ¹¹T. Scholak, T. Wellens, and A. Buchleitner, *J. Phys. B* **44**, 184012 (2011).
- ¹²J. Ye, K. W. Sun, Y. Zhao *et al.*, *J. Chem. Phys.* **136**, 245104 (2012).
- ¹³N. Wu, K. W. Sun, Z. Chang, and Y. Zhao, *J. Chem. Phys.* **136**, 124513 (2012).
- ¹⁴S. J. Xiong, Y. Xiong, and Y. Zhao, *J. Chem. Phys.* **137**, 094107 (2012).
- ¹⁵F. Fassioli *et al.*, *Biophys. J.* **97**, 2464 (2009).
- ¹⁶T. Geyer and V. Helms, *Biophys. J.* **91**, 927 (2006).
- ¹⁷R. Landauer, *IBM J. Res. Dev.* **1**, 223 (1957); M. Buttiker, *Phys. Rev. Lett.* **57**, 1761 (1986).
- ¹⁸S. Datta, *Electronic Transport in Mesoscopic Systems* (Cambridge University Press, 1995).
- ¹⁹H. B. Sun and G. J. Milburn, *Phys. Rev. B* **59**, 10748 (1999).
- ²⁰H. J. Carmichael, *An Open Systems Approach to Quantum Optics* (Springer-Verlag, Berlin, 1993).
- ²¹R. E. Fenna and B. W. Matthews, *Nature (London)* **258**, 573 (1975).
- ²²A. Ben-Shem, F. Frolow, and N. Nelson, *FEBS Lett.* **564**, 274 (2004).
- ²³D. E. Tronrud *et al.*, *Photosynth. Res.* **100**, 79 (2009).
- ²⁴A. Ishizaki and G. R. Fleming, *Proc. Natl. Acad. Sci. U.S.A.* **106**, 17255 (2009).
- ²⁵P. Huo and D. F. Coker, *J. Chem. Phys.* **133**, 184108 (2010).
- ²⁶P. Nalbach, D. Braun, and M. Thorwart, *Phys. Rev. E* **84**, 041926 (2011).
- ²⁷A. Kelly and Y. M. Rhee, *J. Phys. Chem. Lett.* **2**, 808 (2011).
- ²⁸S. Shim *et al.*, *Biophys. J.* **102**, 649 (2012).
- ²⁹M. Schmidt am Busch *et al.*, *J. Phys. Chem. Lett.* **2**, 93 (2011).
- ³⁰G. Ritschel *et al.*, *J. Phys. Chem. Lett.* **2**, 2912 (2011).
- ³¹J. Moix *et al.*, *J. Phys. Chem. Lett.* **2**, 3045 (2011).
- ³²M. Mohseni *et al.*, preprint [arXiv:1104.4812](http://arxiv.org/abs/1104.4812) (2011).
- ³³A. G. Dijkstra and Y. Tanimura, *New J. Phys.* **14**, 073027 (2012).

- ³⁴A. G. Redfield, *IBM J. Res. Dev.* **1**, 19 (1957).
- ³⁵A. G. Redfield, *Adv. Magn. Reson.* **1**, 1 (1965).
- ³⁶W. T. Pollard, A. K. Felts, and R. A. Friesner, *Adv. Chem. Phys.* **93**, 77 (1996).
- ³⁷V. May and O. Kuhn, *Charge and Energy Transfer Dynamics in Molecular Systems*, 2nd ed. (Wiley-VCH, Berlin, 2004).
- ³⁸K. M. Gaab and C. J. Bardeen, *J. Chem. Phys.* **121**, 7813 (2004).
- ³⁹P. Rebentrost *et al.*, *New J. Phys.* **11**, 033003 (2009).
- ⁴⁰J. L. Wu *et al.*, *New J. Phys.* **12**, 105012 (2010).
- ⁴¹H. Haken and G. Strobl, *Z. Phys.* **262**, 135 (1973).
- ⁴²A. Ishizaki and G. R. Fleming, *J. Chem. Phys.* **130**, 234110 (2009).
- ⁴³P. Nalbach and M. Thorwart, *J. Chem. Phys.* **132**, 194111 (2010).
- ⁴⁴W. M. Zhang *et al.*, *J. Chem. Phys.* **108**, 7763 (1998).
- ⁴⁵M. Yang and G. R. Fleming, *Chem. Phys.* **282**, 163 (2002).
- ⁴⁶S. Jang *et al.*, *J. Chem. Phys.* **129**, 101104 (2008).
- ⁴⁷P. Nalbach *et al.*, *New J. Phys.* **13**, 063040 (2011).
- ⁴⁸G. Lindblad, *Commun. Math. Phys.* **48**, 119 (1976).
- ⁴⁹C. W. Gardiner and M. J. Collett, *Phys. Rev. A* **31**, 3761 (1985).
- ⁵⁰C. W. Gardiner, *Quantum Noise* (Springer-Verlag, Berlin, 1991).
- ⁵¹A. Imamoglu and R. J. Ram, *Phys. Lett. A* **214**, 193 (1996).
- ⁵²H. M. Wiseman, *Quantum Semiclass. Opt.* **8**, 205 (1996).
- ⁵³D. W. Utami *et al.*, *Phys. Rev. B* **70**, 075303 (2004).
- ⁵⁴D. W. Utami *et al.*, *Phys. Rev. B* **74**, 014303 (2006).
- ⁵⁵For example, suppose the emitter is a semi-infinite lead consisting of identical pigments with on-site energy E_0 and nearest-neighboring hopping integral g_0 . Then the exciton energy level (single-particle) in the emitter is distributed within the interval $[E_0 - 2g_0, E_0 + 2g_0]$, where the lower bound $E_0 - 2g_0$ represents the chemical potential μ_E . For simplicity, let E_0 be the on-site energy of the entry site (i.e., site 1 in the two-site model and site 8 in the FMO model). It follows that $\bar{n}_E = 1/(e^{2g_0/k_B T} - 1)$. Typically, $g_0 = 50 \text{ cm}^{-1}$, and we have $\bar{n}_E \simeq 0.2(1.6)$ for $T = 77 \text{ K}(300 \text{ K})$.
- ⁵⁶T. Renger and R. A. Marcus, *J. Chem. Phys.* **116**, 9997 (2002).
- ⁵⁷R. Kubo, *J. Math. Phys.* **4**, 174 (1963).
- ⁵⁸S. Mukamel, I. Oppenheim, and J. Ross, *Phys. Rev. A* **17**, 1988 (1978).
- ⁵⁹Y. Tanimura, *J. Phys. Soc. Jpn.* **75**, 082001 (2006).
- ⁶⁰R. X. Xu *et al.*, *J. Chem. Phys.* **131**, 214111 (2009).
- ⁶¹B. Palmieri, D. Abramavicius, and S. Mukamel, *Phys. Chem. Chem. Phys.* **12**, 108 (2010).
- ⁶²L. P. Chen *et al.*, *J. Chem. Phys.* **134**, 194508 (2011).
- ⁶³B. Palmieri, D. Abramavicius, and S. Mukamel, *J. Chem. Phys.* **130**, 204512 (2009).
- ⁶⁴J. Zhu and S. Kais, *J. Phys. Chem. B* **115**, 1531 (2011).
- ⁶⁵T. Brixner *et al.*, *Nature (London)* **434**, 625 (2005).
- ⁶⁶J. Adolphs and T. Renger, *Biophys. J.* **91**, 2778 (2006).
- ⁶⁷E. L. Read *et al.*, *Biophys. J.* **95**, 847 (2008).
- ⁶⁸S. Hoyer *et al.*, *New J. Phys.* **12**, 065041 (2010).
- ⁶⁹D. Manzano, *PLoS ONE* **8**, e57041 (2013).